Micro-structure and morphology characterization of nZVI treated clay with Pb contamination

Abstract:

The increasing use of nanoscale zero-valent iron (nZVI) for soil and groundwater remediation is raising some concerns regarding the potential effect of the soil properties. Numerous laboratory and field studies reveal that an excellent immobilized efficiency of contaminants and enhancement of the contaminated soil by nZVI. Few researches focused on the effect of the nZVI on the micro-structure and morphology of the soil. The overall objective of this study is to explore the particle morphology and micro-structure variation of nZVI treated soil. This study presents a series of microscales experiments on nZVI treated samples, including field emission scanning electron microscopy (FESEM), particle size analysis, mercury injection porosimetry (MIP), optical microscopic analysis and particle shape tests. The dosages of nZVI were used at 0%, 0.2%, 1%, 5% and 10% of the contaminated soil. The morphology tests suggest that the addition of nZVI resulted in the presence of larger particle size, on-particle chained structure, aggregation and network of flocculent structure. The aggregated and bonded soil particles could be one of the mechanisms of the geotechnical characteristics variation and soil enhancement via nZVI.

Key words: Nanoscale zero-valent iron, Aggregation Effect, Morphology, Microstructure, Soil reinforcement

1. Introduction

Nanoscale zero-valent iron (nZVI), with its strong reducing property and high reactivity, have potential for use in remediation of a wide range of hazardous pollutants as indicated. It can react with organic contaminants and heavy metal ions, including Pb^{2+}, Ni^{2+}, As^{2+}, Co^{2+}, Cu^{2+}, CrO_4^{2-}, AsO_4^{3-}, polycyclic aromatic hydrocarbons (PAH) etc. in bench-scale and pilot-scale experiments (Mueller et al. 2012, Singh et al. 2012, Chekli et al. 2016, Tiberg et al. 2016, Wang et al. 2016, Gil-Díaz et al. 2017, Li et al. 2017, Moazeni et al. 2017, Jiang et al. 2018). The nZVI efficiency of aqueous, contaminated groundwater was proved in many literatures. For example, the lab synthesized nZVI - removal of lead ions in aqueous phase was verified the reduced efficiency of 99 % in less than 15 mins (Xi et al. 2010), 96% within 3 hours (Kim et al. 2013) and 96% of heavy metal ions (e.g. copper, arsenic, zinc and nickel) in 10 mins (Li et al. 2017). As mentioned in Liu et al. (2018), the nZVI shows an excellent on immobilization percentage of lead on only 0.2% of nZVI can reach up to 78.8% by testing the consolidated soil, and 95.6% achieved at 10% nZVI (soil wt.). The adsorption, reduction and co-precipitation of ferrites were identified as the predominant process in immobilization (Noubactep 2008, Xi et al. 2010, Tu et al. 2012, Arancibia-Miranda et al. 2014, Wang et al. 2016).

Due to its efficient properties, nZVI has been used for the treatment of contaminated subsurface soil and groundwater. However, the effect of nZVI on the geotechnical properties are still not fully understood. Traditionally, in the applications, nZVI suspension was directly injected into the aquifer or permeable reactive barrier (PRB) to remove contaminants in the target area. However, during this process, nZVI particles are prone to agglomerate mutually or adsorbed onto soil grains, leading to a reduction of surface area (Noubactep 2008, Sarathy et al. 2008, Mueller et al. 2012, Chowdhury et al. 2015, Li et al. 2017). Luo et al. (2012) also found that the utilization of nano aluminium oxide enhanced the unconfined compressive strength of treated sewage sludge ash by the soil slurry preparation while the permeability increased. Ng and Coo

(2015) reported that the permeability of nano copper oxide treated clay significantly decreased using the compacted samples while the liquid limit decreased. It is indicated that the plasticity index reduced with the nanomaterials and liquid limit increased (Ghasabkolaei et al. 2017, Zhou et al. 2018). It should be noted that the effect of different nanomaterials on the soil plasticity need to be on a case by case basis.

Limited information is currently available on the shear strength of soil interacted with chemicals and nanomaterials. It is concluded that the compaction characteristics and compressive strength of the soil were improved by nano clay, nano copper, nano alumina and nano silica (Bahmani et al. 2014, Iranpour and haddad 2016). As for the nZVI treatment of the oil contaminated soil, the significant increases of unconfined shear strength, friction angle and cohesion were observed using the compacted samples (Nasehi et al. 2015). Zhou et al., (2018) and Chen et al., (2018) utilized the different dosages of NZVI to exam the variation of the shear strength and compression behavior of the lead contaminate clay sample which was prepared through a slurry consolidated method. Upon NZVI treatment, a significant shear strength, including the vane shear strength and the friction angle, increased was observed.

To understand how nanomaterials affect it is important, first, to understand how it interacts with the clay-water system (Boardman, 2004). The aggregation of nZVI was considered as a dominant physical effect in the solution (Phenrat et al. 2007). Several potential mechanisms were proposed to explain the increase in shear strength with NZVI is attributed to multi factors, including the immobilization/degradation of heavy metal, changing in the DDL thickness, conglomeration and the aggregated properties of nanomaterials (Ghasabkolaei et al. 2017, Liu et al. 2018, Zhou et al. 2018). The iron oxides was considered as one of the important factors in the formation of pores and aggregates (Regelink et al. 2015). Yet, there is no universally accepted way to characterize the soil structure (Díaz-Zorita et al., 2002). Considering the variation of the geotechnical properties nZVI or nanomaterials treated soil, limited literature update its characterization mechanism how the nZVI reacted with the soil.

The overall objective of this study is to evaluate the nZVI on the characterization of lead contaminated soil. This study presents a series of microstructural assessments, including field emission scanning electron microscopy (FESEM), Laser diffraction analysis, mercury injection porosimetry (MIP), optical microscopic analysis, and particle shape tests at various levels of nZVI (i.e. 0.2%, 1%, 5% and 10%). The samples in this study were prepared following the procedure described by Zhou et al. (2018).

2. Materials and Methods

2.1 Materials

The soil from a local site in Macau was used. The obtained soil was moist sieved through 1 mm and used as matrix material to investigate the multi scale properties of lead-contaminated soil and nZVI treated soil. The Atterberg limits are composed of liquid limit (LL), plastic limit (PL) and plasticity index (PI) defined by the ASTM standard test method - ASTM D4318. The dominant mineral of the natural soil is quartz and its composition consist of Chlorite, illite, kaolinite, anhydrite and plagioclase. The similar results was report in the previous research (Yan and Ma 2010). Moreover, a laser diffraction analysis of the marine clay showed that the soil contained 20% clay, 70% silt, and 10% sand fractions. The liquid limit, plastic limit and plasticity index of the soil was found to be 62%, 32% and 29% respectively. The soil was defined as CL according to the unified soil classification system (USCS).

The based soil (i.e. natural soil) was mixed with distilled water equal to the moisture of 2LL. The contaminated reagent was utilized the lead nitrate (AR) obtained for XiLong Chemical Co. Ltd and mechanically mixed with the natural soil slurry. Notably, the contaminated concentration was 500 mg/kg lead ions (dry weight) and the produced slurry was standing for 48 hours to achieve an equilibrium status. It is noticed that the normal value of lead ions is less than 100 mg/kg(wt.) in a conventional contaminated condition. The composition of the sludge from highly polluted rivers and mining sediments may contain various heavy metal pollutants and high concentration (e.g. Pb-

44.1, Cr-173, Zn-154, Cu-49.7 mg/kg, etc.) (Zhang et al. 2009). However, the superimposed concentration of multiple contaminants is likely to reach even more than 500 mg/kg (wt.).

The treatment was that four dosages (0.2%, 1%, 5% and 10%, by dry weight) of nZVI were added into the contaminated soil slurry while mixed by the electric-agitator for a better dispersion. Nano zero-valent irons (nZVI) as the treated reagent supplied by XiangTian Corp. In order to prevent oxidation of nZVI, the nZVI powders were sealed in a nitrogen-filled packaging. The characterizations of nZVI are as follows: Median radius size of about 50 nm, Purity of 99.9 %, BET Specific surface area (SSA) of 30 m^2/g, Bulk density of 0.48 g/cm^3 and Density of 7.9 g/cm^3. In mixing period, it can be regarded as oxygenated and waterish condition, by which the nZVI can fully react with the ions and clay particles. The time refer to the optimal reaction time (e.g. 5 mins) for the aqueous solution (Kaewbuddee et al. 2016). Considering the soil complexity, it is essential to set the concentration of the treatment reagents matching the contaminants. It is reported that the nZVI performed a higher removal efficiency when the molar ratio of nZVI/lead and nZVI/nitrate is 10 and 4 respectively in the solution(Su et al. 2014, Moazeni et al. 2017). The dosages of nZVI was used as 0.2%, 1%, 5% and 10% (dry density) corresponding to the molar content of nZVI is 15, 75, 370 and 740. Due to the complex minerals in the soil, the removal efficiency was not comparable to that in solution. It may potentially lead to overestimates of the extent of degradation attributable to nZVI. Thus, the ratio of lead vs nZVI represents the proportional condition to excess condition as mentioned in (Zhou et al. 2018).

The produced slurries were consolidated in a double draining consolidation tank at an effective vertical pressure of about 200 kPa. After that, the soils were extracted for the basic property tests, FESEM, particle size tests, MIP, optical microscopic analysis, and particle shape tests.

2.2 Experimental Methods

Slurry consolidated method was used for an efficient reaction among nZVI, water and soil. Furthermore, the consolidated process was identified as anaerobic condition and helpful for simulating the natural process. When the nanoparticles were uniformly dispersed in the semi-dried soil, nanoparticles can fill the void among particles instead of aggregating rapidly. The self-organized structure (e.g. aggregates and gelled networks) of nanomaterial treated soil in the waterish environment has the effective impact on the geotechnical properties (Phenrat et al. 2007).

The microstructures and morphologies of the clay mixtures were analyzed using field emission scanning electron microscope (FESEM, ZEISS Gemini300, Germany). Prior to use, the soil particles were dehydrated by the freeze-vacuum method to remove free water completely. The samples were transferred to the sputter coaters for conductive coating with platinum (Pt) and put it into the scanning electron microscope for examination.

The particle size distribution (PSD) was carried out by a laser diffraction Mastersizer (Malvern 3000, UK), following ASTM D2487 (2006). Before tests, the samples were stirred and homogenized by ultrasonic method at least 5 mins.

The pore size distribution of the consolidated samples was measured by using an Autopore IV 9500 mercury intrusion porosimeter (Micromeritics Corp. USA) with 414 MPa entrance pressure. Considering the negative effect of oven drying method on the microstructures, the freeze-drying method was selected for dehydration (Gallé 2001).The nano-scale pore size distribution is a strong evidence for the micro structure change of undisturbed sample affected by nZVI. The MIP is regarded as an excellent tools to explore the soil pore size distribution with the minimum damage to the pore structure (LAWRENCE 1978, Arvaniti et al. 2015, Li et al. 2015).

The microscopy was conducted by the Nikon microscope (Nikon E200, Japan) equipped with the Nikon DS-L3 image capture system. For the image clearness, microscope images were digitalized. Briefly, a few grammas of samples after pre-

consolidation were selected and diluted with distilled water for 200% moisture content in order to obtain a homogenized soil slurry. The slurries were sealed and maintained at 25°C for 24 hours. Then, the soil slurry was fivefold diluted using ultrapure distilled water and shaken vigorously for 30 s using vortex shaker 3 (IKA, Germany). Each sample were replicated twice at 100× to 1000× magnification. This method would be a few approach for evaluate the micrometer-sized structure under the waterish condition (Phenrat et al. 2007). The sample requires no conductive coating on the specimen under 100X to 1000X magnification (i.e. around 50 -250 μm). This makes it possible to examine the liquid samples and to preserve their natural characteristics and water-steady aggregates for further observation, which is an obvious advantage of this compared to the traditional morphological techniques (e.g. SEM) (Gillott 1970).

The particle shape analysis was performed by the 500 Nano Zephyr LDA (Laser Diffraction Alternative) analyzer (OCCHIO, Belgium). This system consists of a vacuum dispersion device and high-resolution camera with a collimated telecentric lens which can be used for imaging the particles. In this study, the soil particles were smashed and dried by freeze-vacuum method. Size and shape analyses used in this paper have been performed with Occhio's Callisto software which implements best practices of image analysis. Digital image analysis of individual particles has long been recognized as a powerful tool to measure both size and shape parameters and superior to laser diffraction for the irregularly particles, such soil particles (Leroy et al. 2011, Arvaniti et al. 2015).

The specimens were identified using designated notations: NS for natural soil (Virgin soil), PS for Pb^{2+} contaminated soil, and PSN1 for the soil treated with 1% concentration nZVI. The experimental procedure is summarized in Table 1.

Table 1 Experimental design

Equipment	Objective	Scale (μm)	Specimens
Field emission scanning electron microscope (FESEM)	Morphology	1-3	NS, PS, PSN0.2, PSN5, PSN10, NSN5
laser diffraction Mastersizer	Particle size distribution	0.1-1000	NS, PS, PSN0.2, PSN1, PSN5, PSN10
Optical microscope	Micro structure (Waterish)	50-250	NS, PS, PSN1, PSN5, PSN10, NSN5
Mercury intrusion porosimeter (MIP)	Pore size distribution	0.01-100	NS, PS, PSN1, PSN5, PSN10
Nano Zephyr LDA analyzer	Particle shape analysis	25	NS, PS, PSN10

186
187

4. Results and discussion

4.1 FESEM analysis

In order to study the morphological change of particles with great enlargement factor (i.e. up to 1 μm), the particle images from FESEM were shown in Fig. 1. It should be noted that the black background/ shadow is incomplete coating or out of the focal plane because of the spatial structure of the complex shape, rather than a blank area. It provided conclusive proof on the presence of smaller particles and more particle-particle space. The SEM image of natural clay exhibits the superimposition of the dense structure. Examining the image sequence in order of increasing magnification, the fragmentation and crossed structure of contaminated soil may also serve as caused by the lead ions.

After mixing nZVI additive, the microstructure was then conducted to demonstrate the effects of the reaction concentration of nZVI. More cross-linked and conjoint structures were observed. Especially, clastic soil particles become gradually lessened. Meanwhile, it is evident that cross-linked and schistose structures is in the majority, as shown in (f) for NSN5. FESEM images of the treated soil sample show that schistose and laminar texture-like structures formed obviously depending on the nZVI reaction，especially in c) PSN0.2, e) PSN10 and (f) NSN5. The schistose structures of the larger dosage become less evident and degree of reticulation appears to increase.

This may be attributed to the formation of elemental lead and ferrite via redox reaction and the aggregation of nZVI (Fig. 6), which changes the morphology of particle surface and connections. The morphological results were consistent with the research reported by Xi et al. (2010) and Mar Gil-Díaz et al., (2014). The variation of morphology should be ascribed to the flocculation of nZVI-Pb-soil and the formation of ferrite/ oxides/hydroxides with nZVI additive. The results suggest that the use of nZVI in the soil can produce more structural connection, which could be considered as the main reason of the engineering properties. This is consistent with the observation of the particle shape, pore size and soil micro-structure. All these results are supported

by FESEM observations and highlight the fact that the geotechnical properties changes are due to a reorganization of the particles leading to fabric changes (Souli et al. 2008).

It cannot be denied that the change of the particle morphology could have an impact on the geotechnical properties. However, Young et al. (2001) questioned that the aggregates through the morphological technologies was the result of how we choose to observe them. Thus, the pore size distribution was considered as the key evidence to support the assumption of the micro-structures change.

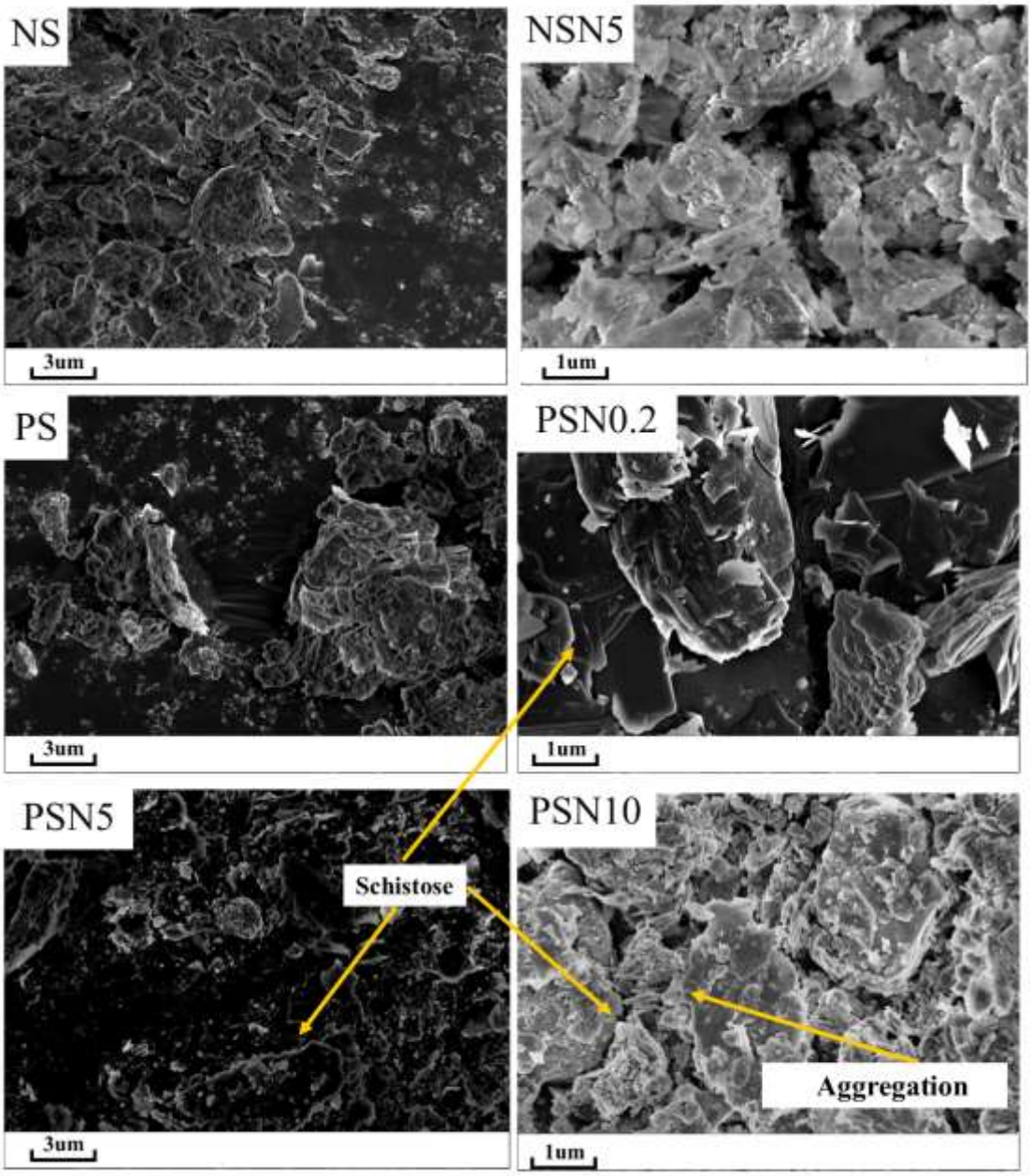

Fig. 1 FESEM results of nZVI treated soil at different dosages: (a) Natural soil (NS); (b) NSN5; (c) PS; (d) PSN0.2, (e) PSN5 and (f) for PSN10

226

227 *4.2 Particle size distribution*

228 Fig. 2 shows the particle size distribution of each sample and pure nZVI. The particle
229 size distribution shows the scale impact from 0.1 to 2000 μm. Four typical curves are
230 shown for a clear view. The particle size distribution of contaminated soil tends to more
231 fine particles than that of natural soil. This could be due to the rearrangement of the
232 double layer or the reacted precipitation (Helios Rybicka et al. 1995, Schmitz et al. 2004,
233 Du et al. 2015). On the other hand, with the increasing concentration of nZVI, the
234 particle size distribution curves shifted to the right, which means that larger size
235 particles appeared. The addition of nZVI from 1% to 10% results in an increment 15.6%
236 of sand percentage. Meanwhile, the clay-size percentage of specific soil decrease from
237 26.8% to 19.6%. Once the nZVI was added into the water, some large-scale particles or
238 structures (with D_{50} = 22 um) appeared due to the nature of aggregation and magnetism.
239

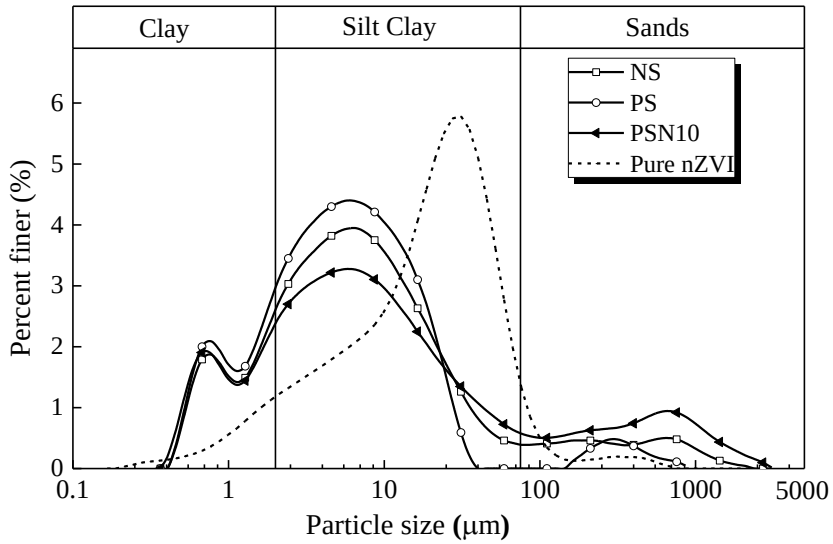

240

241 **Fig. 2.** Particle size distribution of treated sample and nZVI in the solution

242

243 The results of the specific diameter are shown in Fig. 3. The D_{10}, D_{50} and D_{90}
244 proceeded in a gradual manner with the inclusion of nZVI dosage. It is noted that the
245 D_{10} and D_{50} slightly decrease with the presence of nZVI less than 1%. The D_{10} was
246 around 1 um on the whole and increase efficiently with the 5% and 10 % nZVI (24.2%

247 increment). Furthermore, the trend of D_{50} was consistent with that of D_{10}. The D_{50} of
248 10% nZVI has a 19.5% growth. As considering the D_{90}, the value has a little change
249 when the dosage is less than 5%. With the introduction of 10% nZVI, the D_{90} increases
250 significantly from 25 to 321 μm. However, it has a larger relative standard deviation
251 which means the non-uniformity of the large particles. Possibly, it could result from the
252 high reactivity of nZVI and hence the excess nZVI lead to drastic formation of the
253 cross-linked aggregations and bounded structure. Previous studies reported that the
254 nanoparticles tend to form much larger (e.g., microscale) aggregates in the absence of
255 surface-active dispersants. The changes in clay- and sand-sized particle percentages in
256 the stabilized soils are dominantly attributed to both short-term flocculation formation
257 and long-term oxidation reactions (Nalbantoglu and Tuncer 2001, Tran et al. 2014, Xia
258 et al. 2017). Both mechanisms of nZVI in the soil could result in a higher percentage
259 of particle or bounded aggregations (Phenrat et al. 2007, Li et al. 2008, Moazeni et al.
260 2017). He et al. (2008) indicated that different particle sizes show different tendency to
261 aggregate.

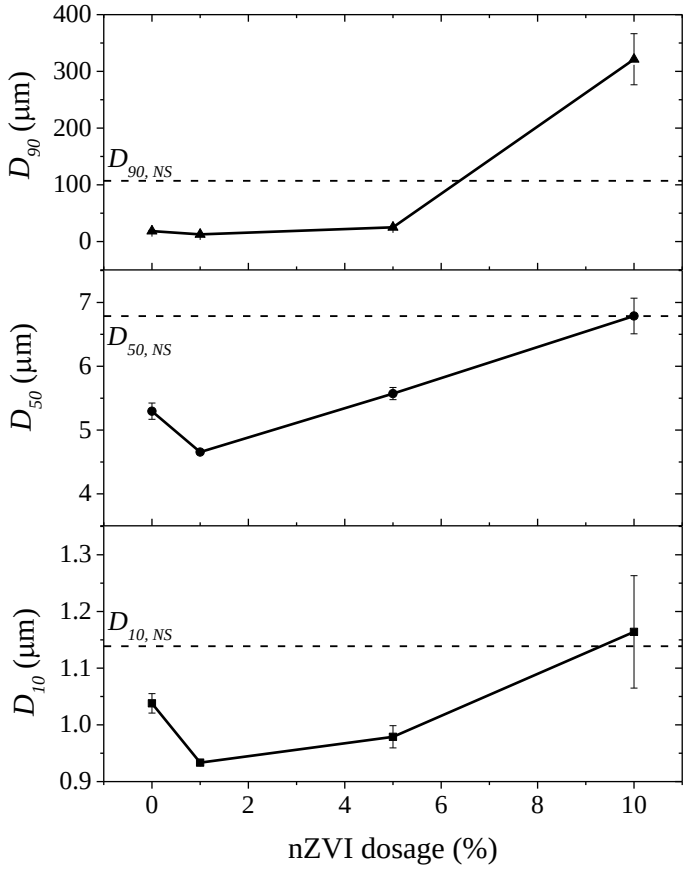

Fig. 3. Particle size diameter results from the PSD tests Error bars represent RSD (n = 5, Relative Standard Deviation)

4.3 Pore size distribution

In the following, the results are analyzed with respect to the evolution of the pore size distribution. The samples were treated with different dosages and consolidated, by which the final void ratio could be various due to the change of geotechnical properties. Hence, this section focuses on the change of pore size and explore the variation of soil structure. In all the soil cases, the pore size distributions show an intrusion at a pressure corresponding to a threshold diameter close to 0.003 µm and up to 10 µm.

The Fig. 4 presents the mercury intrusion and extrusion curves for treated and untreated soil. Five typical curves are shown in this figure for a visible and distinguishable view. With such a porous structure, mercury cannot intrude into larger pores until the applied pressure is sufficient to force mercury to go through smaller

277 throats. As a result, the volume of these larger pores is counted as the volume of smaller
278 throats. This is referred to as the “accessibility effect” (Diamond 2000) The larger pores
279 that are accessible to mercury through smaller throats are called ink-bottle pores. And,
280 the smaller throats are called throat pores. As a result, the MIP measurement provides
281 an underestimation of the volume of the large pore and an overestimation of the volume
282 of the small pore. According to Ramakrishanan et al. (1998) self-consistent pore-
283 body/pore-throat ratios can be obtained from the measured hysteresis between the
284 intrusion and extrusion curves (Anovitz and Cole 2015). Therefore, for all samples, a
285 large hysteresis is presented between mercury intrusion and extrusion curves. This
286 phenomenon could be explained by poor connectivity of pore network
287 Due to the initial vacuum procedure, the extrusion efficiency was calculated by the
288 cumulative extrusion /cumulative intrusion value at around 110 kPa. It represents the
289 ratio between the volume of the connective pore and that of total pore. The mercury
290 extrusion curves of the nZVI treated samples present more significant differences with
291 that of untreated sample. The mercury extrusion efficiency increases with nZVI dosage
292 to 22.14% (PS), 27.25% (PSN1), 28.79% (PSN5) and 42.66% (PSN10) respectively. It
293 indicates that most of the intruded mercury is still trapped in the soil due to the ink
294 bottle and throat effect, which shows a poor connectivity of the natural soil. However,
295 it can be noted that the proportion of the connective pores increases with the nZVI and
296 hence that the change of the inter-aggregate connection can be deduced.
297 It indicated that the slightly increasing segment of the intrusion (i.e. late stage of the
298 curve) could be one of the effective methods to distinguish the intra-aggregate pores
299 (Sakhaee-Pour and Bryant 2014). The turning point was calculated as the maximum
300 tangent slope. The late stages proportion of NS and PS are less than 1%. However, that
301 of PSN1, PSN5, PSN10 and NSN5 are around 9.6%, 10.9%, 14.2% and 10.2%,
302 respectively. Thus, it was acceptable that the inclusion of the nZVI has a great influence
303 on the intra-aggregate pores. The intra-aggregate pores were highly correlated with the
304 addition of the nanomaterials.

From the further analysis, it is noted that the pore volume and the pore size reduce with the introduction of nZVI in both. The increase of the initial threshold pore entrance diameter was observed as well, which was used as one of the evaluation criteria of the pores (Burton et al. 2015). It has been well documented that the cross-linked structure of the nZVI dispersion could create an impermeable barrier and thus plug the pore spaces and thereby lead to the decrease of pore size (Phenrat et al. 2007, He et al. 2010, Chowdhury et al. 2015, Li et al. 2016). The decrease of pore volume and pore diameter distribution is considered to generate a more compact structure in the soil skeleton, and hence has a gain in enhancement. The inter-aggregate and pores have remarkable effects on the strength properties of soils, as a result, the soil samples stabilized with higher content of nZVI have superior mechanical performances than those stabilized with lower content of nZVI (Horpibulsuk et al. 2009, Jiang et al. 2014, 2016).

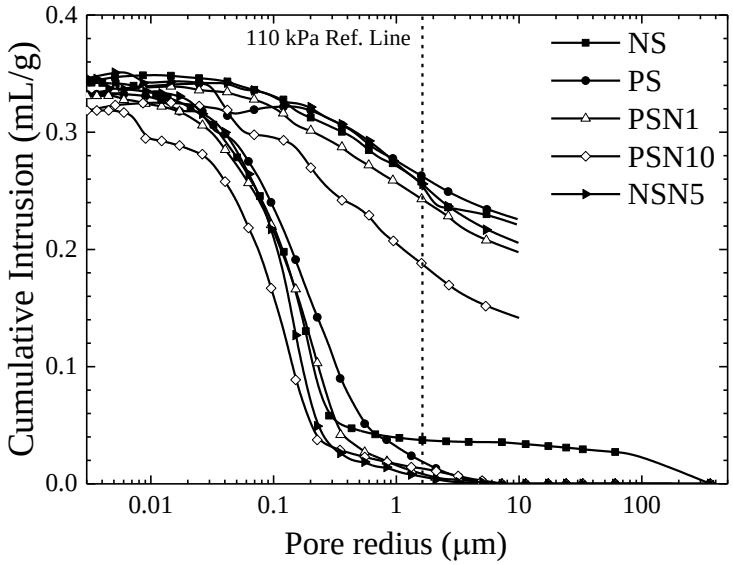

Fig. 4. Mercury intrusion and extrusion curves of the samples

Fig. 5 present the MIP pore size distribution curves for the natural soil and treated soil. It presents that the main peak intensity ranges from 0.1-0.4 μm with a dominant peak. The curve shape shows a major peak and a sub-peak intrusion in some cases. That means the Soil-Pore structures dominated the soil skeleton with the addition. The

variation of pore size distribution could be summarized as the dual-structure (i.e. interaggregate pores and intra-aggregate pores) (Li and Zhang 2009).

As the comparison to the NS and PS results, it indicates that the addition of lead contaminants may lead to generate a larger pore (0.3-0.8 μm) and the peak was not obvious which could be attributed to the thickness of the diffused double layer. Lead ions in soil may break the charge balance between the soil particles due to the exchangeable valent cations and result in the increase in the repulsive force of the contaminated soil particles. The presence of cations can affect the particle stability of nZVI particles and result in more large pores among the aggregates (He and Zhao 2007).

Compared with the natural soil, contaminated soil, PSN1, PSN5, PSN10 and NSN5, the curves shift to the left, which means the increase in the smaller pores. With the presence of 1% nZVI, the proportion of the pores with 0.3-0.7 μm decreases. The curves of PSN5 and PSN10 have the similar trend with that of PSN1, such as 0.05-0.25 μm for PSN5 and 0.12-0.5 μm for PSN10. As expected, the pore diameter decreases with the nZVI addition from 1% to 10%, showing a porosity refinement due to the nano pore of nZVI, nano-scale aggregation/precipitate. The nZVI aggregation of clay particles tended to change the portion of both interaggregate pores and intra-aggregate pores. The aggregated structure of nZVI dispersion could create a porous structure and thus plug the pore spaces. This is because the nanomaterials (i.e. nZVI) or aggregates acted as the bonding connections or filler in the void or the agglomeration (Chandni Dipak and Srirama 2015, Ghasabkolaei et al. 2017). Ng and Coo (2015) indicates that the largest pore size reduced by 20% when clay was mixed with 4% nano copper oxide. The stiff aggregates form a strong connection to carry the compression force, which could be the reasons for the nZVI enhancement (Taha and Taha 2012, Zhou et al. 2018). Iron oxides have the ability to form strong bindings with clay, silt and sand particles, meaning that iron oxides can provide sorption sites for organic substances on the surfaces of these otherwise low to moderately reactive particles (Sei et al. 2002). The iron oxides could enhance the formation of small-scale aggregates and soil pores (Lu

et al. 2014, Regelink et al. 2015). The Soil-nZVI structure (i.e. interaggregate pores) could be one of the main reasons for the reduction of the large pores.

Due to the nano-scale materials, the pore size can be predicted as the increasing proportion of micrometer-size or nanometer-size. Especially, a sub-peak intrusion, less than 0.01 μm scale, is observed for the PSN10 and NSN5. It can be assumed that the excess nZVI may result in the formation of the unreacted nZVI aggregation because of the pores of the aggregates. Due to the ink bottle effect and throat effect, the volume of the pores (less than 10 nm) could be overestimated. However, this issue is out of the scope of this study. Thus, this tendency was acceptable. The intra-aggregate pores are regarded as the nZVI-Pore structures. It confirmed that the extreme excess nZVI could be not easily dispersed and generate the nZVI aggregates.

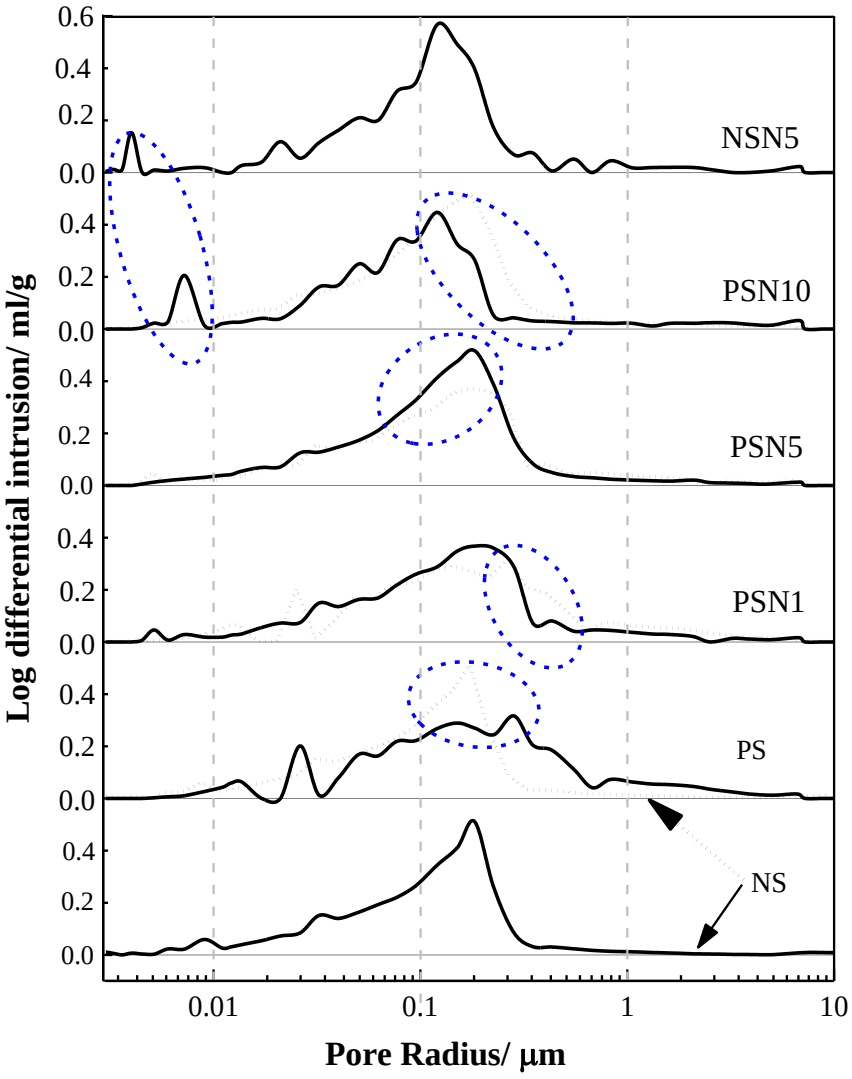

Fig. 5. Variations of differential intrusion with respect to pore radius.

4.4 Optical microscopic analysis

For clarifying the aggregation of nZVI in the waterish condition, the optical microscopic analysis was conducted. This is one of the qualitative methods for studying the arrangements of micro-structures in the soil (She et al. 2018). Although the SEM technology has been a common method for the morphological analysis. However, some of the samples were sensitive to the air or dried condition and exhibited different structures, such as the soil. The water-steady structures are vital to the soil skeleton.

Fig. 6 notes the micrographs of pure nZVI in the distilled water under 1000X magnification. After shaking vigorously, the existing structure could be regarded as a strong bond among the soil particles. The formation of large aggregates and larger chain-like fractal aggregates (around 50 um) was observed in the nZVI suspension with/without shaking. The size of the observed aggregation is consistent with the particle size distribution of pure nZVI in the water.

Although the size of the aggregates (micron-sized) is significantly larger than the origin scale of nZVI (Nanometer-sized), previous studies reported that the nZVI tend to form much larger aggregates under nanoscale magnifications in the dispersants (Li et al. 2008). Some of the nZVI aggregates in the water are easy to be disturbed by mechanical disturbance because the aggregation forces are the van der Waals and magnetic forces (Phenrat et al. 2007, Kim et al. 2013). The observation of the loosely-boned cluster still dominate the chain-like and network structure (He et al. 2010, Dorjee et al. 2014, Chowdhury et al. 2015, Li et al. 2016). Chekli et al. (2016) shows similar characterization evidences of nZVI. This observation could be one of the fundamental evidences for the nZVI-soil aggregations.

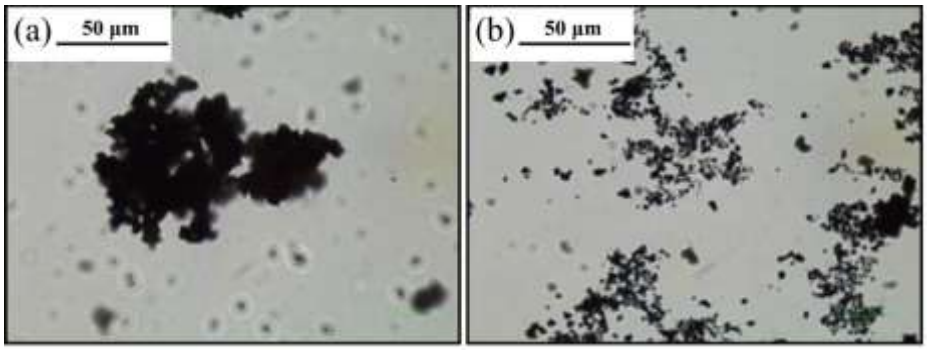

Fig. 6. Micrographs of pure nZVI under 1000X magnifications; (a) the origin nZVI in the water, (b) the nZVI in the water after shaken vigorously for 180 s

Fig. 7 shows the digitalized micrographs of soil mixture at 100X magnification. Aiming to obtain the convictive results and nZVI effects, the referral sample (i.e. NSN5) was added in this series of microscopic tests. The black area was the soil particles and the white area was the water. The suspensions of the samples in the water shows the fabric structures. The images of NS show a homogeneous state of soil particles and few aggregates. The micrographs of PS show a few flocculent aggregations in the horizon and the particles are dispersive. With the nZVI treatment, the flocculation of the treated samples become clearer, and large particles and more chain-like aggregates like the nZVI structure were observed, by which it would be helpful to enhance the connection between the particles. As the increase of the nZVI dosage, the aggregates (i.e. Black area) become more distinguishable and the particle size increases. Compared to the NS and NSN5, the inclusion of 5% nZVI has an efficient flocculation on the soil dispersion and thereby more aggregates and connections are detected. This observation could be a potential mechanism of the micro-structure properties of the wetting soil in the presence of nZVI.

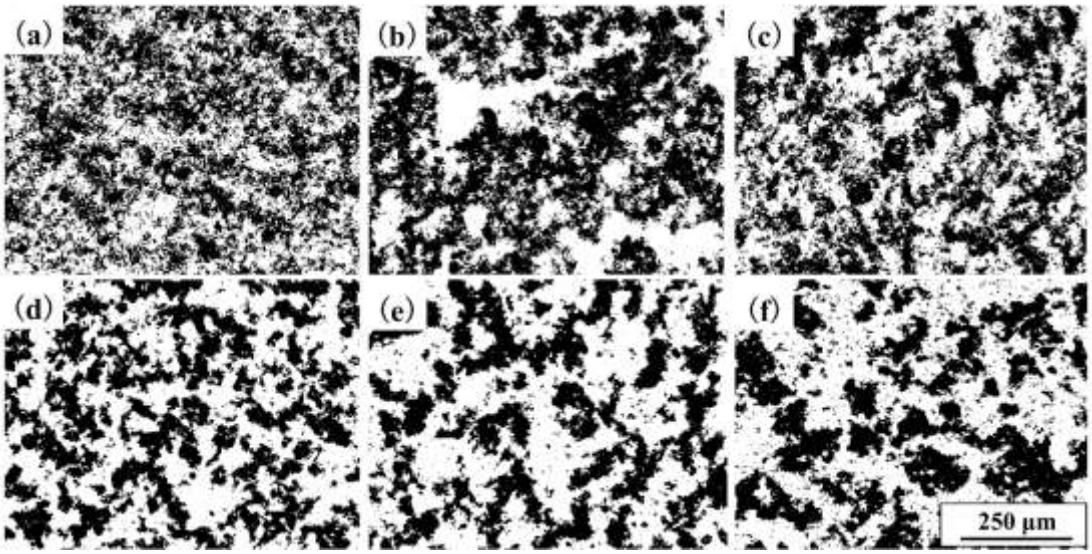

Fig. 7. Digitalized micrographs of the reacted specimens at 100X magnification: (a) NS, (b) PS, (c) PSN1, (d) PSN5, (e) PSN10 and (f) for NSN5

Fig. 8 shows the original state of NS, PSN10 and NSN5 under optical microscope with 1000X magnification. The scattered fraction of the soil particles was in the majority. As for the nZVI treated sample, the aggregations and larger particles can be monitored, which exhibited the cross-linked and chained structure compared to that of the NS. The morphology of the PSN10 particles exhibits the fractal and chain-like aggregates. This could be a solid evidence for the nZVI effect on the soil structure under waterish condition.

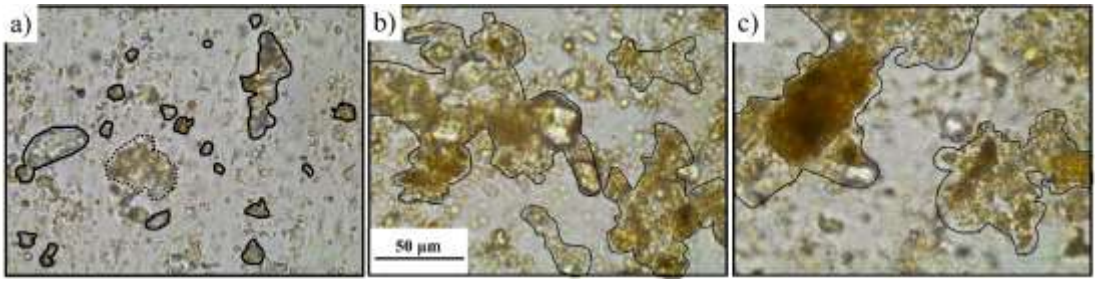

Fig. 8. Micrographs of reaction specimens 1000X magnification: (a) NS, (b) PSN10, (c) NSN5

These results show a consistent tendency, in which a clear microstructural change is detected at microscopic scale with the nZVI addition. As expected, the formation of larger chain- like aggregates from the individual micrometer-sized aggregates was observed in the Fig. 7 and Fig. 8. It is reasonable that nZVI treated sample exhibit a

higher percentage of larger-sized aggregates, which suggests that the more nZVI dosage results in the acceleration of aggregates. It is an available route to estimate the geotechnical properties on aqueous condition through the microscope. As for the quantitative evaluation of soil microstructure. The structure of consolidated sample is not only affected by microstructural changes, but the compaction. It would explain the aggregation effect of nZVI and the increase of particle size in the PSD results. As for the chain-like aggregation formation, that may influence the soil skeleton structure and the engineering properties of nZVI treated soil.

4.5 Particle shape analysis

In addition to exploring the structural variations, the change of particle shape would influence the engineering properties in a sub micro scale (i.e. dozens of microns, 25μm). Hence, the particle shape photograph was conducted for exploring the effect of nZVI. Considering the soil particles shape analysis, some typical optical pictures were selected randomly from hundreds of particle shape images within reasonable scale. Due to the incompleteness by the vacuum dispersion and the strong bound structure, two or several soil particles cemented to each other may be observed as one particle sometimes. However, for the particle size measurement technique, the obtained results are different from the waterish condition (i.e. particle size analysis) and the dry condition. Here, this section is focused on the change of the particle shape rather than the particle size comparison.

The digitalized images of the particle shape selected from the similar particle size are shown in Fig. 9. The results show chained structures on the surface of aggregation or particle as the main variation with nZVI addition. It has demonstrated a consistent trend with the observed structure of nZVI treated samples under the microscope. It can be identified that some of particles could be bonded and the size close to about 50 micrometers because the incomplete dispersion, which is better to exhibit the cohesive combination. Furthermore, it should be noted that the vacuum dispersion could break

458 the loose connection (e.g. the “tentacle” of the particles) before the tests. A possible
459 reason for this phenomenon is that the interacted production and precipitation of the
460 nZVI on the particle surface and the magnetic nature of nZVI could accelerate the
461 aggregation effect. It can be assumed that the chained structure on the particle surface
462 had linked each other in the undisturbed condition, by which the aggregate interlock
463 capacity (Micro effect) will become larger and result in the increase of strength (Macro
464 effect). In this case, the connectivity pore (MIP observed) could appear among the
465 aggregates with the chained structure.
466

467
468 **Fig. 9.** Digitalized particle shape images of the NS, PS and PSN10.
469
470 The main results of particle shape parameters are plotted in the Fig. 10. The global
471 surface concavity index (GSCI) was defined by the overall concavity of the projected
472 area of the particle. The roughness was the ratio of smooth reference to the particle
473 projection area. The smooth reference is defined by the inscribed circles tangent to each
474 point of the particle projection outline with a radius whose roughness value is the
475 percentage greater than the maximum inscribed circle. The volume-equivalent diameter
476 (D_v) was that the diameter of a sphere having the same volume as the particle (Wadell
477 1932).
478 From the images and parameter analysis, the variation of the particle shape can easily

be observed. For the nZVI addition for the treatment, the volume-equivalent diameter, global surface concavity and roughness increase significantly. Meanwhile, the friction angles increase, and the increment rate of the strength was similar to that of the parameters. As expected, this change may be one of the mechanisms of the increase of friction and soil resistance. Some literature stated that the increase of the particle roughness and cementations could lead to an increase of the friction angle using a sand sample (Cho et al. 2006, Rousé et al. 2008, Hassanlourad et al. 2011, Stark et al. 2014). This could be another solid evidence for the nZVI effect on the soil structure and have an impact on the mechanical characteristics.

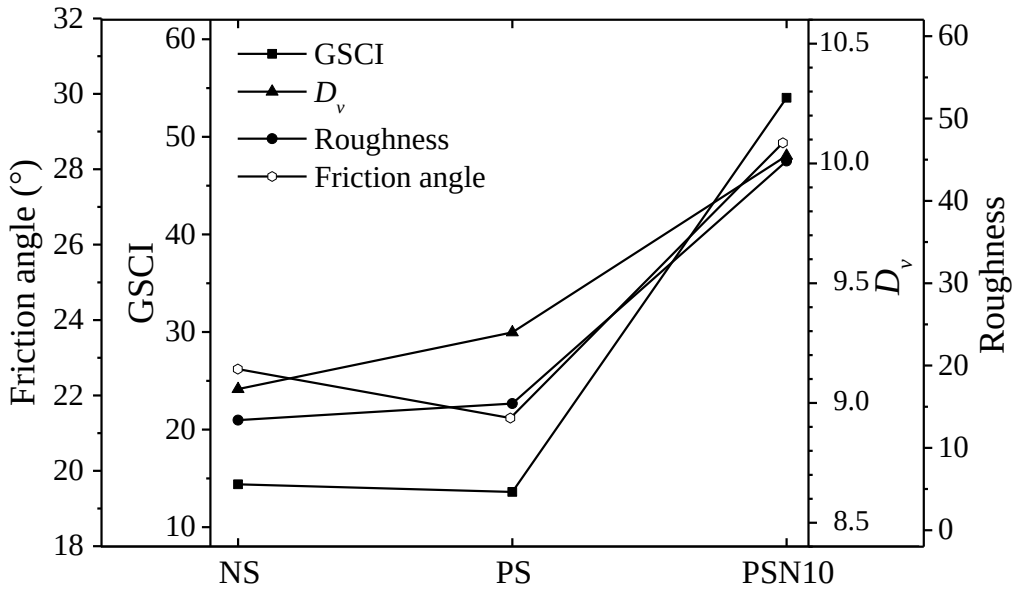

Fig. 10. Main shape parameters of the particle shape and friction angle

5. Summary and conclusions

In this study, an investigation of the nZVI effect on the microstructure was examined. The FESEM analysis shows that the nZVI treated samples presented more schistose and aggregated structures. The nZVI addition results in an increase of particle size and finer pore size, which represented the formation of the dense structure with the nanomaterials. The optical microscopic analysis and particle shape experiments

demonstrates that the nZVI addition induced aggregations and chain-like structures that could be bonded to a network structure in the consolidated sample. Meanwhile, the nZVI influence the soil skeletal structure and the engineering properties of nZVI treated soil. The particle shape analysis confirmed the change of the particles morphology. Some possible explanations for the soil enhancement are deduced including: the larger particle size, formation of chained aggregation, cross-linked on-surface structures, larger particle roughness. The findings would be beneficial for understanding the mechanism and engineering behaviors of nZVI treated soil. The mechanism needs to be investigated in depth.

Acknowledgement

The authors gratefully acknowledge the financial supports from Science and Technology Development Fund, Macao S.A.R (FDCT, Code 193/2017/A3) and the University of Macau Research Fund (MYRG2017-00198-FST).

References

Anovitz, L.M., and Cole, D.R. 2015. Characterization and Analysis of Porosity and Pore Structures. Reviews in Mineralogy and Geochemistry, **80**(1): 61–164. doi:10.2138/rmg.2015.80.04.

Arancibia-Miranda, N., Baltazar, S.E., García, A., Romero, A.H., Rubio, M.A., and Altbir, D. 2014. Lead removal by nano-scale zero valent iron: Surface analysis and pH effect. Materials Research Bulletin, **59**: 341–348. doi:10.1016/j.materresbull.2014.07.045.

Arvaniti, E.C., Juenger, M.C.G., Bernal, S.A., Duchesne, J., Courard, L., Leroy, S., Provis, J.L., Klemm, A., and De Belie, N. 2015. Determination of particle size, surface area, and shape of supplementary cementitious materials by different techniques. Materials and Structures, **48**(11): 3687–3701. doi:10.1617/s11527-014-0431-3.

526 ASTM D4318, ASTM D 4318-10, and D4318-05, A. 2005. Standard Test Methods
527 for Liquid Limit, Plastic Limit, and Plasticity Index of Soils. Report, **04**(March
528 2010): 1–14. doi:10.1520/D4318-10.
529 Astm, and International, A. 2006. Standard Practice for Classification of Soils for
530 Engineering Purposes (Unified Soil Classification System). ASTM Standard
531 Guide, **D5521-05**: 1–5. doi:10.1520/D2487-11.
532 Bahmani, S.H., Huat, B.B.K., Asadi, A., and Farzadnia, N. 2014. Stabilization of
533 residual soil using SiO2nanoparticles and cement. Construction and Building
534 Materials, **64**: 350–359. Elsevier Ltd. doi:10.1016/j.conbuildmat.2014.04.086.
535 Burton, G.J., Pineda, J.A., Sheng, D., and Airey, D. 2015. Microstructural changes of
536 an undisturbed, reconstituted and compacted high plasticity clay subjected to
537 wetting and drying. Engineering Geology, **193**: 363–373. Elsevier B.V.
538 doi:10.1016/j.enggeo.2015.05.010.
539 Chandni Dipak, S., and Srirama, D. 2015. A review of stabilization of expansive soils
540 by using nanomaterials. 50th INDIAN GEOTECHNICAL CONFERENCE 17th
541 – 19th DECEMBER 2015, (December): 8.
542 Chekli, L., Bayatsarmadi, B., Sekine, R., Sarkar, B., Shen, A.M., Scheckel, K.G.,
543 Skinner, W., Naidu, R., Shon, H.K., Lombi, E., and Donner, E. 2016. Analytical
544 characterisation of nanoscale zero-valent iron: A methodological review.
545 Analytica Chimica Acta, **903**: 13–35. Elsevier Ltd.
546 doi:10.1016/j.aca.2015.10.040.
547 Cho, G.-C., Dodds, J., and Santamarina, J.C. 2006. Particle Shape Effects on Packing
548 Density, Stiffness, and Strength: Natural and Crushed Sands. Journal of
549 Geotechnical and Geoenvironmental Engineering, **132**(5): 591–602.
550 doi:10.1061/(ASCE)1090-0241(2006)132:5(591).
551 Chowdhury, A.I.A., Krol, M.M., Kocur, C.M., Boparai, H.K., Weber, K.P., Sleep,
552 B.E., and O'Carroll, D.M. 2015. NZVI injection into variably saturated soils:
553 Field and modeling study. Journal of Contaminant Hydrology, **183**: 16–28.

554 Elsevier B.V. doi:10.1016/j.jconhyd.2015.10.003.
555 Diamond, S. 2000. Mercury porosimetry An inappropriate method for the
556 measurement of pore size distributions in cement-based materials. **30**: 1517–
557 1525.
558 Dorjee, P., Amarasiriwardena, D., and Xing, B. 2014. Antimony adsorption by zero-
559 valent iron nanoparticles (nZVI): Ion chromatography-inductively coupled
560 plasma mass spectrometry (IC-ICP-MS) study. Microchemical Journal, **116**: 15–
561 23. Elsevier B.V. doi:10.1016/j.microc.2014.03.010.
562 Du, Y.J., Fan, R.D., Reddy, K.R., Liu, S.Y., and Yang, Y.L. 2015. Impacts of
563 presence of lead contamination in clayey soil-calcium bentonite cutoff wall
564 backfills. Applied Clay Science, **108**: 111–122. doi:10.1016/j.clay.2015.02.006.
565 Gallé, C. 2001. Effect of drying on cement-based materials pore structure as identified
566 by mercury intrusion porosimetry - A comparative study between oven-,
567 vacuum-, and freeze-drying. Cement and Concrete Research, **31**(10): 1467–1477.
568 doi:10.1016/S0008-8846(01)00594-4.
569 Ghasabkolaei, N., Janalizadeh Choobbasti, A., Roshan, N., and Ghasemi, S.E. 2017.
570 Geotechnical properties of the soils modified with nanomaterials: A
571 comprehensive review. Archives of Civil and Mechanical Engineering, **17**(3):
572 639–650. Politechnika Wrocławska. doi:10.1016/j.acme.2017.01.010.
573 Gil-Díaz, M., Pinilla, P., Alonso, J., and Lobo, M.C. 2017. Viability of a
574 nanoremediation process in single or multi-metal(loid) contaminated soils.
575 Journal of Hazardous Materials, **321**: 812–819. Elsevier B.V.
576 doi:10.1016/j.jhazmat.2016.09.071.
577 Gillott, J.E. 1970. Fabric of Leda clay investigated by optical, electron-optical, and X-
578 ray diffraction methods. Engineering Geology, **4**(2): 133–153. doi:10.1016/0013-
579 7952(70)90009-8.
580 Hassanlourad, M., Salehzadeh, H., and Shahnazari, H. 2011. Undrained triaxial shear
581 behavior of grouted carbonate sands. International Journal of Civil Engineering,

582 **9**(4): 307–314.
583 He, F., and Zhao, D. 2007. Manipulating the size and dispersibility of zerovalent iron
584 nanoparticles by use of carboxymethyl cellulose stabilizers. Environmental
585 Science and Technology, **41**(17): 6216–6221. doi:10.1021/es0705543.
586 He, F., Zhao, D., and Paul, C. 2010. Field assessment of carboxymethyl cellulose
587 stabilized iron nanoparticles for in situ destruction of chlorinated solvents in
588 source zones. Water Research, **44**(7): 2360–2370. Elsevier Ltd.
589 doi:10.1016/j.watres.2009.12.041.
590 He, Y.T., Wan, J., and Tokunaga, T. 2008. Kinetic stability of hematite nanoparticles:
591 The effect of particle sizes. Journal of Nanoparticle Research, **10**(2): 321–332.
592 doi:10.1007/s11051-007-9255-1.
593 Helios Rybicka, E., Calmano, W., and Breeger, A. 1995. Heavy metals
594 sorption/desorption on competing clay minerals; an experimental study. Applied
595 Clay Science, **9**(5): 369–381. doi:10.1016/0169-1317(94)00030-T.
596 Horpibulsuk, S., RACHAN, R., and RAKSACHON, Y. 2009. Role of Fly Ash on
597 Strength and Microstructure Development in Blended Cement Stabilized Silty
598 Clay. Soils and Foundations, **49**(1): 85–98. doi:10.3208/sandf.49.85.
599 Iranpour, B., and haddad, A. 2016. The influence of nanomaterials on collapsible soil
600 treatment. Engineering Geology, **205**: 40–53. doi:10.1016/j.enggeo.2016.02.015.
601 Jiang, D., Zeng, G., Huang, D., Chen, M., Zhang, C., Huang, C., and Wan, J. 2018.
602 Remediation of contaminated soils by enhanced nanoscale zero valent iron.
603 Environmental Research, **163**(November 2017): 217–227. Elsevier Inc.
604 doi:10.1016/j.envres.2018.01.030.
605 Jiang, M., Zhang, F., Hu, H., Cui, Y., and Peng, J. 2014. Structural characterization of
606 natural loess and remolded loess under triaxial tests. Engineering Geology, **181**:
607 249–260. Elsevier B.V. doi:10.1016/j.enggeo.2014.07.021.
608 Jiang, N.-J., Du, Y.-J., Liu, S.-Y., Wei, M.-L., Horpibulsuk, S., and Arulrajah, A.
609 2016. Multi-scale laboratory evaluation of the physical, mechanical, and

microstructural properties of soft highway subgrade soil stabilized with calcium carbide residue. Canadian Geotechnical Journal, **53**(3): 373–383. doi:10.1139/cgj-2015-0245.

Kaewbuddee, C., Chanpiwat, P., Kidkhunthod, P., and Wantala, K. 2016. Lead adsorption behaviours on nanoscale zero valent irons (nZVI) coupled with rice husk MCM-41. Sains Malaysiana, **45**(7): 1155–1167.

Kim, S.A., Lee, K., Park, Y., and Shea, P.J. 2013. Removal of Pb (II) from aqueous solution by a zeolite – nanoscale zero-valent iron composite. Chemical Engineering Journal, (217): 54–60. doi:10.1016/j.cej.2012.11.097.

LAWRENCE, G.P. 1978. Stability of Soil Pores During Mercury Intrusion Porosimetry. Journal of Soil Science, **29**(3): 299–304. doi:10.1111/j.1365-2389.1978.tb00777.x.

Leroy, S., Dislaire, G., Bastin, D., and Pirard, E. 2011. Optical analysis of particle size and chromite liberation from pulp samples of a UG2 ore regrinding circuit. Minerals Engineering, **24**(12): 1340–1347. Elsevier Ltd. doi:10.1016/j.mineng.2011.06.006.

Li, J., Rajajayavel, S.R.C., and Ghoshal, S. 2016. Transport of carboxymethyl cellulose-coated zerovalent iron nanoparticles in a sand tank: Effects of sand grain size, nanoparticle concentration and injection velocity. Chemosphere, **150**: 8–16. Elsevier Ltd. doi:10.1016/j.chemosphere.2015.12.075.

Li, J. shan, Xue, Q., Wang, P., and Li, Z. ze. 2015. Effect of lead (II) on the mechanical behavior and microstructure development of a Chinese clay. Applied Clay Science, **105**–**106**: 192–199. Elsevier B.V. doi:10.1016/j.clay.2014.12.030.

Li, S., Wang, W., Liang, F., and Zhang, W.X. 2017. Heavy metal removal using nanoscale zero-valent iron (nZVI): Theory and application. Journal of Hazardous Materials, **322**: 163–171. Elsevier B.V. doi:10.1016/j.jhazmat.2016.01.032.

Li, X., and Zhang, L.M. 2009. Characterization of dual-structure pore-size distribution of soil. Canadian Geotechnical Journal, **46**(2): 129–141.

638 doi:10.1139/T08-110.
639 Li, X.Q., Cao, J., and Zhang, W.X. 2008. Stoichiometry of Cr(VI) immobilization
640 using nanoscale zero valent iron (nZVI): A study with high-resolution X-ray
641 photoelectron spectroscopy (HR-XPS). Industrial and Engineering Chemistry
642 Research, **47**(7): 2131–2139. doi:10.1021/ie061655x.
643 Liu, F., Zhou, W. huan, and Yi, S. 2018. Immobilization of Pb in Soil Using NZVI
644 Nanoparticles: Effects on Vane Shear Strength. *In* GeoChina 2018:
645 Transportation and Geotechniques: Materials, Sustainability and Climate.
646 Springer International Publishing. pp. 174–185. doi:10.1007/978-3-319-95768-5.
647 Lu, S.G., Malik, Z., Chen, D.P., and Wu, C.F. 2014. Porosity and pore size
648 distribution of Ultisols and correlations to soil iron oxides. Catena, **123**: 79–87.
649 Elsevier B.V. doi:10.1016/j.catena.2014.07.010.
650 Luo, H.-L., Hsiao, D.-H., Lin, D.-F., and Lin, C.-K. 2012. Cohesive Soil Stabilized
651 Using Sewage Sludge Ash/Cement and Nano Aluminum Oxide. International
652 Journal of Transportation Science and Technology, **1**(1): 83–100. Tongji
653 University and Tongji University Press. doi:10.1260/2046-0430.1.1.83.
654 Mar Gil-Díaz, M., Pérez-Sanz, A., Ángeles Vicente, M., and Carmen Lobo, M. 2014.
655 Immobilisation of Pb and Zn in soils using stabilised zero-valent iron
656 nanoparticles: Effects on soil properties. Clean - Soil, Air, Water, **42**(12): 1776–
657 1784. doi:10.1002/clen.201300730.
658 Moazeni, M., Ebrahimi, A., Rafiei, N., and Pourzamani, H.R. 2017. Removal of Lead
659 Ions from Aqueous Solution by Nano Zero-Valent Iron (nZVI). Health Scope,
660 **6**(2): e40240. doi:10.17795/jhealthscope-40240.
661 Mueller, N.C., Braun, J., Bruns, J., Černík, M., Rissing, P., Rickerby, D., and
662 Nowack, B. 2012. Application of nanoscale zero valent iron (NZVI) for
663 groundwater remediation in Europe. Environmental Science and Pollution
664 Research, **19**(2): 550–558. doi:10.1007/s11356-011-0576-3.
665 Nalbantoglu, Z., and Tuncer, E.R. 2001. Compressibility and hydraulic conductivity

666 of a chemically treated e×pansive clay. Canadian Geotechnical Journal, **38**(1):
667 154–160. doi:10.1139/cgj-38-1-154.
668 Nasehi, S.A., Uromeihy, A., Morsali, A., and Nikudel, M.R. 2015. Use of nanoscale
669 zero-valent iron to improve the shear strength parameters of gas oil contaminated
670 clay. **5**(2): 161–175.
671 Ng, C.W.W., and Coo, J.L. 2015. Hydraulic conductivity of clay mixed with
672 nanomaterials. Canadian Geotechnical Journal, **52**(6): 808–811. doi:10.1139/cgj-
673 2014-0313.
674 Noubactep, C. 2008. A critical review on the process of contaminant removal in Fe0-
675 H2O systems. Environmental Technology, **29**(8): 909–920.
676 doi:10.1080/09593330802131602.
677 Phenrat, T., Saleh, N., Sirk, K., Tilton, R.D., and Lowry, G. V. 2007. Aggregation and
678 sedimentation of aqueous nanoscale zerovalent iron dispersions. Environmental
679 Science and Technology, **41**(1): 284–290. doi:10.1021/es061349a.
680 Regelink, I.C., Stoof, C.R., Rousseva, S., Weng, L., Lair, G.J., Kram, P., Nikolaidis,
681 N.P., Kercheva, M., Banwart, S., and Comans, R.N.J. 2015. Linkages between
682 aggregate formation, porosity and soil chemical properties. Geoderma, **247**–**248**:
683 24–37. Elsevier B.V. doi:10.1016/j.geoderma.2015.01.022.
684 Rousé, P.C., Fannin, R.J., and Shuttle, D.A. 2008. Influence of roundness on the void
685 ratio and strength of uniform sand. Géotechnique, **58**(3): 227–231.
686 doi:10.1680/geot.2008.58.3.227.
687 Sakhaee-Pour, A., and Bryant, S.L. 2014. Effect of pore structure on the producibility
688 of tight-gas sandstones. AAPG Bulletin, **98**(4): 663–694.
689 doi:10.1306/08011312078.
690 Sarathy, V., Tratnyek, P.G., Nurmi, J.T., Baer, D.R., Amonette, J.E., Chun, C.L.,
691 Penn, R.L., and Reardon, E.J. 2008. Aging of iron nanoparticles in aqueous
692 solution: Effects on structure and reactivity. Journal of Physical Chemistry C,
693 **112**(7): 2286–2293. doi:10.1021/jp0777418.

694 Schmitz, R.M., Schroeder, C., and Charlier, R. 2004. Chemo-mechanical interactions
695 in clay: A correlation between clay mineralogy and Atterberg limits. Applied
696 Clay Science, **26**(1–4 SPEC. ISS.): 351–358. doi:10.1016/j.clay.2003.12.015.
697 Sei, J., Jumas, J.C., Olivier-Fourcade, J., Quiquampoix, H., and Staunton, S. 2002.
698 ROLE OF IRON OXIDES IN THE PHOSPHATE ADSORPTION
699 PROPERTIES OF KAOLINITES FROM THE IVORY COAST. Clays and Clay
700 Minerals, **50**(2): 217–222. Available from http://dx.doi.org/.
701 She, W., Cao, X., Zhao, G., Cai, D., Jiang, J., and Hu, X. 2018. Experimental and
702 numerical investigation of the effect of soil type and fineness on soil frost heave
703 behavior. Cold Regions Science and Technology, **148**(February): 148–158.
704 Elsevier. doi:10.1016/j.coldregions.2018.01.015.
705 Singh, R., Misra, V., and Singh, R.P. 2012. Removal of Cr(VI) by nanoscale zero-
706 valent iron (nZVI) from soil contaminated with tannery wastes. Bulletin of
707 Environmental Contamination and Toxicology, **88**(2): 210–214.
708 doi:10.1007/s00128-011-0425-6.
709 Souli, H., Fleureau, J.M., Trabelsi Ayadi, M., and Besnard, M. 2008. Physicochemical
710 analysis of permeability changes in the presence of zinc. Geoderma, **145**(1–2):
711 1–7. doi:10.1016/j.geoderma.2008.02.014.
712 Stark, N., Hay, A.E., Cheel, R., and Lake, C.B. 2014. The impact of particle shape on
713 the angle of internal friction and the implications for sediment dynamics at a
714 steep, mixed sand-gravel beach. Earth Surface Dynamics, **2**(2): 469–480.
715 doi:10.5194/esurf-2-469-2014.
716 Su, Y., Adeleye, A.S., Zhou, X., Dai, C., Zhang, W., Keller, A.A., and Zhang, Y.
717 2014. Effects of nitrate on the treatment of lead contaminated groundwater by
718 nanoscale zerovalent iron. Journal of Hazardous Materials, **280**: 504–513.
719 Elsevier B.V. doi:10.1016/j.jhazmat.2014.08.040.
720 Taha, M.R., and Taha, O.M.E. 2012. Influence of nano-material on the expansive and
721 shrinkage soil behavior. Journal of Nanoparticle Research, **14**(10).

722 doi:10.1007/s11051-012-1190-0.
723 Tiberg, C., Kumpiene, J., Gustafsson, J.P., Marsz, A., Persson, I., Mench, M., and
724 Kleja, D.B. 2016. Immobilization of Cu and As in two contaminated soils with
725 zero-valent iron - Long-term performance and mechanisms. Applied
726 Geochemistry, **67**: 144–152. Elsevier Ltd.
727 doi:10.1016/j.apgeochem.2016.02.009.
728 Tran, T.D., Cui, Y.J., Tang, A.M., Audiguier, M., and Cojean, R. 2014. Effects of
729 lime treatment on the microstructure and hydraulic conductivity of Héricourt
730 clay. Journal of Rock Mechanics and Geotechnical Engineering, **6**(5): 399–404.
731 Elsevier Ltd. doi:10.1016/j.jrmge.2014.07.001.
732 Tu, Y.J., Chang, C.K., You, C.F., and Wang, S.L. 2012. Treatment of complex heavy
733 metal wastewater using a multi-staged ferrite process. Journal of Hazardous
734 Materials, **209**–**210**: 379–384. Elsevier B.V. doi:10.1016/j.jhazmat.2012.01.050.
735 Wadell, H. 1932. Volume, shape, and roundness of rock particles. The Journal of
736 Geology, **40**(5): 443–451.
737 Wang, W., Hua, Y., Li, S., Yan, W., and Zhang, W. xian. 2016. Removal of Pb(II)
738 and Zn(II) using lime and nanoscale zero-valent iron (nZVI): A comparative
739 study. Chemical Engineering Journal, **304**: 79–88. Elsevier B.V.
740 doi:10.1016/j.cej.2016.06.069.
741 Xi, Y., Mallavarapu, M., and Naidu, R. 2010. Reduction and adsorption of Pb2+in
742 aqueous solution by nano-zero-valent iron - A SEM, TEM and XPS study.
743 Materials Research Bulletin, **45**(10): 1361–1367.
744 doi:10.1016/j.materresbull.2010.06.046.
745 Xia, W.Y., Feng, Y.S., Jin, F., Zhang, L.M., and Du, Y.J. 2017. Stabilization and
746 solidification of a heavy metal contaminated site soil using a hydroxyapatite
747 based binder. Construction and Building Materials, **156**: 199–207. Elsevier Ltd.
748 doi:10.1016/j.conbuildmat.2017.08.149.
749 Yan, W.M., and Ma, Y. 2010. Geotechnical characterization of Macau marine

750 deposits. Engineering Geology, **113**(1–4): 62–69. Elsevier B.V.
751 doi:10.1016/j.enggeo.2010.03.001.
752 Young, I.M., Crawford, J.W., and Rappoldt, C. 2001. New methods and models for
753 characterising structural heterogeneity of soil. Soil and Tillage Research, **61**(1–
754 2): 33–45. doi:10.1016/S0167-1987(01)00188-X.
755 Zhou, W.-H., Chen, Y.-Z., Liu, F., and Yi, S. 2018. Experimental Study on the
756 Strength Characteristics of Lead Contaminated Soil with NZVI Treatment. *In*
757 GeoShanghai 2018 International Conference: Geoenvironment and Geohazard.
758 Springer Singapore. pp. 273–279. doi:10.1007/978-981-13-0128-5.
759